UCLA
UCLA Electronic Theses and Dissertations

Title

Polarization-Informed Non-Line-of-Sight Imaging on Diffuse Surfaces

Permalink

https://escholarship.org/uc/item/67k4v6h2

Author

Hassan, Bakari

Publication Date

2019

Peer reviewed|Thesis/dissertation

UNIVERSITY OF CALIFORNIA

Los Angeles

Polarization-Informed Non-Line-of-Sight Imaging on Diffuse Surfaces

A thesis submitted in partial satisfaction

of the requirements for the degree

Master of Science in Electrical & Computer Engineering

by

Bakari Hassan

2019

ABSTRACT OF THE THESIS

Polarization-Informed Non-Line-of-Sight Imaging on Diffuse Surfaces

by

Bakari Hassan

Master of Science in Electrical & Computer Engineering

University of California, Los Angeles, 2019

Professor Achuta Kadambi, Chair

Non-line-of-sight (NLOS) imaging has relevance in search & rescue, medical imaging, remote sensing, and robotics. Although NLOS methods are maturing, NLOS with normal cameras generally requires special occluders in the scene to remove light transport ambiguity. In this paper, it is shown that polarization reveals unique information about occluded environments, and computation in the polarization domain has sparsity benefits that aid the inverse problem. This is demonstrated via non-line-of-sight imaging on rough, everyday surfaces such as office/home walls. If successful, it has the potential to enable direct and indirect occluded light source discrimination and passive shape recovery of hidden objects via shape from polarization.

The thesis of Bakari Hassan is approved.

Johnathan Chau-Yan Kao

Vwani P Roychowdhury

Achuta Kadambi, Committee Chair

University of California, Los Angeles

2019

To my grandmother ...

This isn't my thesis

It's her thesis

TABLE OF CONTENTS

LIST OF FIGURES

ACKNOWLEDGMENTS

Thanks to all my famliy, friends, and mentors who have pushed me to be the engineer I am today.

CHAPTER 1

Introduction

Previous papers in Non-Line-of-Sight (NLOS) imaging have focused on active methods limited to use of complex cameras. Although passive methods enable use of ordinary visible cameras, they suffer from light transport ambiguity and commonly require occluders placed relative to the camera to gain more information about the scene. This paper shows that incorporating polarization with the Cook-Torrance shader introduces sparsity to the light transport matrix (LTM), enabling the passive recovery of scenes occluded by rough surfaces that are intractable for a purely intensity-based method (Figure 1.1).

This paper has three key technical contributions:

1. Presents a simple modification to the Cook-Torrance shader that incorporates polarization

2. Discusses how this introduces sparsity to the LTM and simplifies the inverse model

3. Demonstrates polarization-informed NLOS by reconstructing images on a monitor hidden by an occluder

The paper is structured as follows. Related work in polarization imaging, polarization scattering, and NLOS imaging is discussed in 2, Section 3 covers the model used to realize diffuse reflection Mueller matrices and derive light transport. Section 4 is an overview of the experiment setup and data collection processes. Results are discussed in section 5 with conclusions in section 6.
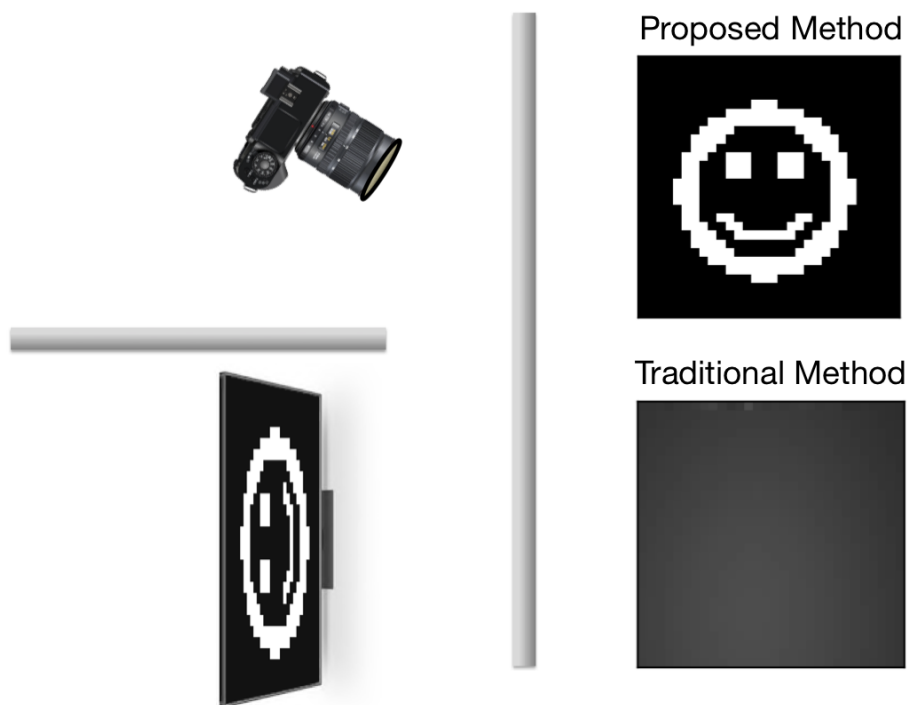
Figure 1.1: The method proposed herein recovers an occluded scene while traditional methods fail.

CHAPTER 2

Related Work

The framework and applications relevant to NLOS polarization imaging span many fields. In this section, we first provide an overview of related passive NLOS imaging methods followed by a summary of polarization scattering models used for imaging with rough surfaces.

Active NLOS imaging Active methods have been the main focus to date and include both coherent and incoherent light sources that exploit the memory effect and time of flight respectively. Smith et. al tracked moving NLOS objects using speckle pattern from coherent sources [1]. Katz et. al uses speckle correlations for NLOS imaging through scattering media and recovers spatial information via phase retrieval [2]. Heide et. al developed an active method that uses factored light transport to perform NLOS imaging of partially occluded scenes [3]. A wave-based method was recently proposed that records the photon time of flight using single-photon avalanche diodes but solves the NLOS imaging problem in the frequency domain rather than the time domain [4]. This offers computation speed advantages at the cost of oscillatory artifacts from the wave field.

Passive NLOS imaging Passive NLOS imaging is attractive over due to its simplicity and low cost. However, due to less control over the environment, problems are generally faced with increased model ambiguity. A dense LTM with limited localized structure poses a challenge for the inverse problem. Since such a matrix means many light sources map to a single camera pixel, the optimization problem has many degrees of freedom, and converging to the correct solution becomes increasingly challenging. Field of view occluders have been used to provide more structure to the columns of the LTM and remove inverse problem ambiguity [5]. While most algorithms have used light reflecting from a wall to perform

NLOS imaging, Bouman et. al developed a NLOS method to image around corners using small variations in radiance on the floor rather than imaging radiance changes on a wall [6]. Data-driven methods using convolutional neural networks to process shadows cast by geometric primitives in rooms have been used to alleviate the need for advanced sensors as well [7].

Polarization imaging   Polarization has many applications in the field of computer vision due to the additional information it provides that is generally invisible to the human eye. It has been used in underwater environments to perform de-scattering and improve camera contrast [8]. Kadambi et. al used the surface normal information encoded in polarization state to realize high-fidelity normal maps for low-cost 3D scanners by increasing depth resolution [9]. Cross-polarization is also useful for non-invasive medical imaging, as polarizing filters can be used to remove specular reflections and observe sub-surface skin scattering signatures [10]. The additional dimensionality in polarization that encodes more information about the environment comes with the cost of requiring more complex models to fully understand its behavior.

Diffuse reflections & polarization   Modeling the effects of scattering on polarization is not as easy as particle-based scattering models. The complete scattering model evaluates the volumetric integral equation (VIE) to solve for a 2x2 scattering amplitude matrix which transforms the incident polarization state to the reflected state. Bruce presents a method to derive the scattering matrix and a Mueller for scattered light from two-dimensional diffuse surfaces using the reduced Rayleigh equations [11]. However, it relies on surface statistics being view-independent and does not extend well to grazing incidence viewing angles. Numerical methods that solve for Mueller matrices for all incidence angles have also been developed [12]. Since VIE approaches are commonly intractable for complex scenes, there are several approximations. The Kirchhoff approximation assumes Gaussian surface statistics and is compatible with surface features larger than the wavelength. Thorsos identified failure cases for Gaussian surfaces and found that the surface correlation length is highly

influential on the model's validity rather than facet radius of curvature as previously thought [13]. Monte Carlo methods have been used to bridge the VIE with the well-known specular effects on polarization via stochastic ray tracing [14, 13]. However, extensive ray tracing is time-consuming a generally precludes near real-time operation. Given the goal of this paper is to develop a method that is near real-time and is extendable to a variety of rough surfaces encountered in industrial and domestic environments, these models all fall short either due to high complexity or over-simplicity. For a comprehensive survey of polarization scattering models and augmentations, see [15].

Computer graphics shaders   Computer graphics provides a wealth of computationally efficient and flexible shading algorithms due to the high demand for speed and flexibility in 3D modeling. Popular shaders such as Phong and Blinn-Phong work well for specular reflections but break-down for diffuse reflections [16, 17]. Others such as the Lambert and Oren-Nayar shaders specialize in diffuse reflections [18]. The Cook-Torrance model bridges these two categories by assuming rough surfaces are composed of specular microfacets [19]. This model is well-suited for our problem, as specular polarization reflections are well-known and characterized by the Fresnel relations. For this reason, the Cook-Torrance shader is chosen as the light transport model for NLOS polarization.

CHAPTER 3

Proposed Method

3.0.1 Cook-Torrance Intensity Shader

Cook & Torrance introduce a model to emulate the BRDF of a material by assuming specular highlights are created by a set of microfacets, and diffuse reflection is a result of localized inter-reflection [19]. They derive a BRDF expression that determines the measured intensity reflected from a single scene point to a chosen observation position. Their BRDF expression is composed of two types of illumination which are in terms of the scene geometry shown in Figure 3.1. The first is ambient illumination, which is considered to be independent of viewing angle. The second is the combined illumination from multiple scene light sources that produces both specular and diffuse reflections.

Within the second term (the summation), the first part is the intensity created by a light source of intensity $I_\ell^{(i)}$, solid angle σ, and with a cosine loss of $\mathbf{L} \cdot \mathbf{N}$ due to its angle of incidence. The second term is a linear combination of the specular and diffuse reflectances, R_s and R_d with the weights satisfying $\gamma_s + \gamma_d = 1$.

$$I^{(r)} = R_a I_a^{(i)} + \sum_{\ell=1}^{L} \sigma_\ell (L_\ell \cdot N)[\gamma_s R_s(L_\ell) + \gamma_d R_d]I_\ell^{(i)} \tag{3.1}$$

where $I_\ell^{(i)}$ is light source ℓ's incident intensity, and $I^{(r)}$ is the total reflected intensity. Here, only R_s is a function of the light source since the ambient and diffuse reflectances are perspective-independent.
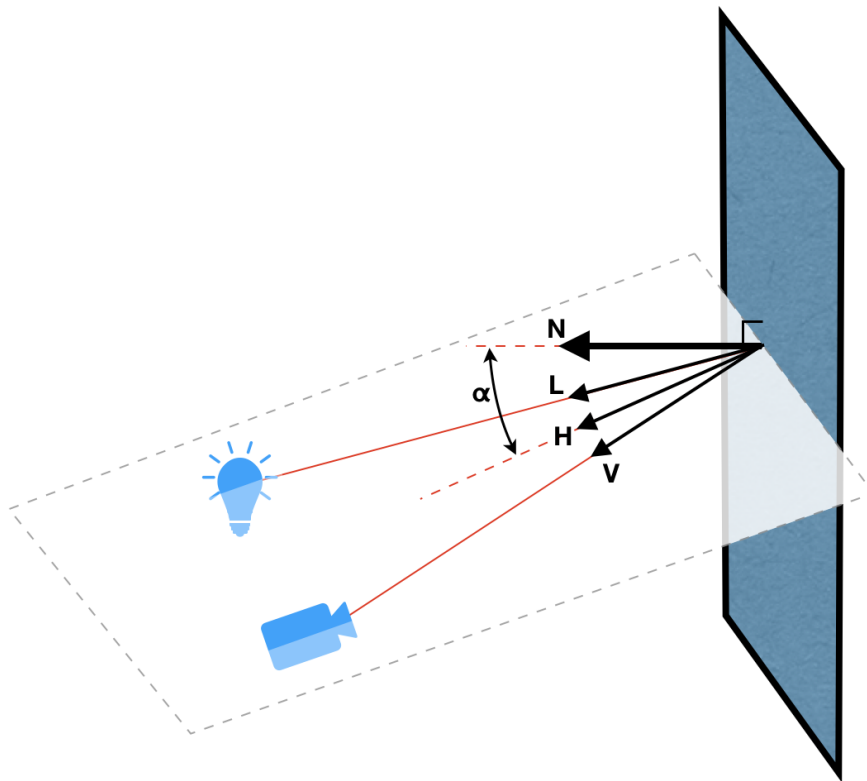
Figure 3.1: Geometry used in the Cook-Torrance model

3.0.2 Polarization-Based Cook-Torrance Model

In our proposed method, we leverage the Cook-Torrance shader's assumption that rough surfaces' specular reflections are achieved via microfacets. For NLOS polarization, we're interested in Stokes parameters rather than intensities, and we're interested in Mueller matrices rather than reflectance values. By making the replacements accordingly, 3.1 can be tailored, resulting in the Cook-Torrance shader for polarization:

$$\mathbf{S^{(r)}} = \mathbf{R_a S_a^{(i)}} + \sum_{\ell=1}^{L} \sigma_\ell \left[\mathbf{L}_\ell \cdot \mathbf{N} \right] \left[\gamma_s \mathbf{R_s} + \gamma_d \mathbf{R_d} \right] \mathbf{S_\ell^{(i)}} \tag{3.2}$$

where $\mathbf{R_a}$, $\mathbf{R_s}$, and $\mathbf{R_d}$ are ambient, specular, and diffuse reflection Mueller matrices respectively; $\mathbf{S^{(i)}}$ and $\mathbf{S^{(r)}}$ are the incident and reflected Stokes vectors respectively.

Ambient Mueller Matrix The Cook-Torrance model assumes the ambient reflectance is uniform for all viewing directions and surface orientations. Therefore, we assume the ambient component is an ideal depolarizer, which preserves the intensity and eliminates all directional polarization components:

$$\mathbf{R_a} = \begin{bmatrix} 1 & 0 & 0 & 0 \\ 0 & 0 & 0 & 0 \\ 0 & 0 & 0 & 0 \\ 0 & 0 & 0 & 0 \end{bmatrix} \tag{3.3}$$

Diffuse Mueller Matrix For diffuse light source reflections, we choose a Mueller matrix that acts as both an attenuator and a partial depolarizer with an attenuation coefficient ϵ_d and a depolarizing coefficient δ_d both less than or equal to unity:

$$\mathbf{R_d} = \begin{bmatrix} \epsilon_d & 0 & 0 & 0 \\ 0 & \epsilon_d \delta_d & 0 & 0 \\ 0 & 0 & \epsilon_d \delta_d & 0 \\ 0 & 0 & 0 & \epsilon_d \delta_d \end{bmatrix} \tag{3.4}$$

8

Specular Mueller Matrix   To represent specular microfacet reflections, we express $\mathbf{R_s}$ as a function of a Fresnel reflection Mueller matrix $\mathbf{R_f}$ with factors G (geometry function) and D (normal distribution function)accounting for intensity losses due to geometric shadowing & masking and the effective surface area contributing to the specular reflection due to the microfacet assumption. Since the Fresnel equations are in terms of s and p polarization, we apply two frame rotations $\mathbf{R_\theta}$ pre- and post-reflection so the x axis is parallel to the wall, and the y axis is perpendicular. The specular Mueller matrix $\mathbf{R}_s$ is:

$$\mathbf{R_s} = \frac{DG}{\pi(\mathbf{N}\cdot\mathbf{L})(\mathbf{N}\cdot\mathbf{V})}\mathbf{R}_\theta\big(-\theta\big)\mathbf{R}_f\mathbf{R}_\theta\big(\theta\big) \tag{3.5}$$

where the denominator accounts for intensity losses due to the relative positions of the light source and the viewer. The terms D, G, $\mathbf{R_f}$ and $\mathbf{R_\theta}$ in Equation 3.5 are defined as:

$$D = \frac{1}{m^2\cos^4\alpha}e^{-[\tan\alpha/m]^2} \tag{3.6}$$

$$G = \min\left\{1, \frac{2(\mathbf{N}\cdot\mathbf{H})(\mathbf{N}\cdot\mathbf{V})}{(\mathbf{V}\cdot\mathbf{H})}, \frac{2(\mathbf{N}\cdot\mathbf{H})(\mathbf{N}\cdot\mathbf{L})}{(\mathbf{V}\cdot\mathbf{H})}\right\} \tag{3.7}$$

$$\mathbf{R_f} = \begin{bmatrix} r_p^2 + r_s^2 & r_p^2 - r_s^2 & 0 & 0 \\ r_p^2 - r_s^2 & r_p^2 + r_s^2 & 0 & 0 \\ 0 & 0 & 2r_s r_p & 0 \\ 0 & 0 & 0 & 2r_s r_p \end{bmatrix} \tag{3.8}$$

$$\mathbf{R_\theta}\big(\theta\big) = \begin{bmatrix} 1 & 0 & 0 & 0 \\ 0 & \cos(2\theta) & \sin(2\theta) & 0 \\ 0 & -\sin(2\theta) & \cos(2\theta) & 0 \\ 0 & 0 & 0 & 1 \end{bmatrix} \tag{3.9}$$

where m is a roughness parameter in the normal distribution function which must be chosen, α is the angle between the light-view bisector and the wall patch normal vector, and r_p and r_s are the Fresnel coefficients for p and s polarization respectively. For each ray

incident with the wall, the rotation angle is related to the inner product of the light ray's polarization frame x axis, $\mathbf{vx}$, and its projection onto the x-y plane $\mathbf{v_{xy}}$. Rodrigues vector rotation about the propagation vector is used to make this rotation through an angle θ:

$$\theta = \arctan \frac{\mathbf{v}_{xy}^T(\mathbf{k} \times \mathbf{v_x})}{\mathbf{v}_{xy}^T(\mathbf{v_x} - \mathbf{k}^T\mathbf{v_x})} \tag{3.10}$$

This completes the forward model that maps a scene light's polarization state to a camera measurement. In order to recover an unknown light source's polarization state, the inverse problem must be solved.

3.0.3 Recovering Light Source Polarization

Equation 3.2 indicates that the polarization state measured by each camera pixel is linear combination of each light source's Stokes vector with the Mueller reflection matrix for the wall patch seen by that pixel plus a constant ambient illumination component $\mathbf{C}$. Transformations are represented by a Cook-Torrance reflectance tensor $\mathbf{R}' \in \mathcal{R}^{V \times 4 \times 4}$ composed of Mueller matrices, and the polarization image $\mathcal{S}$ is:

$$\mathcal{S} = \sum_{\ell=1}^{L} \begin{bmatrix} \mathbf{R}'_{1,\ell} \\ \mathbf{R}'_{2,\ell} \\ \vdots \\ \mathbf{R}'_{V,\ell} \end{bmatrix} \mathbf{S}_\ell^{(\mathbf{i})} + \mathbf{C} \tag{3.11}$$

where $\mathbf{R}'_{v,\ell} = [\mathbf{L}_\ell \cdot \mathbf{N}][\gamma_s \mathbf{R_s} + \gamma_d \mathbf{R_d}]$ and $\mathcal{S} \in \mathcal{R}^{V \times 4 \times 1}$.

We assume the number of camera pixels exceeds the number of light sources (pixels on the monitor), and that this is an overdetermined linear system. We seek the minimal-energy solution which is one in which the algorithm recovers the original image with intensities as small as possible. Therefore, we use Tikhonov regularization to recover the light source's polarization properties with the Tikhonov matrix $\mathbf{\Gamma}$ chosen as a diagonal matrix with every fourth entry equal to 1 to penalize high-intensity solutions.

Equation 3.11 can be vectorized to get the standard $\mathbf{y} = \mathbf{Ax} + \mathbf{b}$ affine transform by

stacking the Cook-Torrance reflectance tensors horizontally and the light source Stokes vectors vertically. Assuming no ambient light ($\mathbf{b} = \mathbf{0}$) and the monitor's maximum degree of polarization ρ_{max} is known (0.6 for this paper), the optimization problem can be expressed:

$$
\begin{aligned}
P1: \quad &\underset{\mathbf{x}}{\text{minimize}} \quad \parallel \mathbf{Ax} - \mathbf{y} \parallel_2^2 + \lambda \parallel \mathbf{\Gamma x} \parallel_2^2 \\
&\text{subject to} \quad\quad\quad 0 \le s_0 \le I_{max} \\
&\quad\quad\quad\quad\quad -s_0\rho_{max} \le s_1 \le s_0\rho_{max} \\
&\quad\quad\quad\quad\quad -s_1^2 \le s_2^2 \le s_0^2 - s_1^2
\end{aligned}
\tag{3.12}
$$

where I_{max} is the monitor's maximum pixel brightness, and s_n is the nth component of the ℓth light source's Stokes vector. The first four constraints enforce valid Stokes parameter, while the final constraint enforces the law of conservation of energy as a function of the assumed degree of polarization. The Tikhonov matrix is defined according to the index i:

$$
\text{diag}(\mathbf{\Gamma})_i = \begin{cases} 1 & \mod(i, 4) = 0 \\ 0 & \text{otherwise} \end{cases} \quad \text{for } i = 0, \dots, 4L - 1
\tag{3.13}
$$

Since P1 is a separable optimization objective that must be minimized with constraints, it can be solved quickly and efficiently using Alternating Direction Method of Multipliers (ADMM) [20]. If the objective is $f(\mathbf{x})$, the augmented Lagrangian is:

$$
L(\mathbf{x}, \mathbf{y}) = f(\mathbf{x}) + \frac{1}{2}\mu_k \mathbf{c}^T \mathbf{c} - \mathbf{y}^T \mathbf{c}
\tag{3.14}
$$

where $\mathbf{c}$ is a penalizer for constraint violation, μ_k is an increasing penalty weight, and $\mathbf{y}$ is an estimate of the Lagrange multiplier that is refined at each iteration. Now the algorithm iteratively performs partial updates of dual variables $\mathbf{x}$ and $\mathbf{z}$ until the convergence criteria have been satisfied. For NLOS polarization, only $f(\mathbf{x})$ is used analytically, and $g(\mathbf{z})$ is a user defined function that imposes constraints on $\mathbf{z}$ by resetting each invalid entry to a valid range. After iteration k, the values at iteration k + 1 are:

$$
\mathbf{x}^{k+1} = \text{argmin } L(\mathbf{x}, \mathbf{z^k}, \mathbf{y^k})
\tag{3.15}
$$

11

$$\mathbf{z}^{k+1} = \text{impose constraints on } \mathbf{x}^{k+1} \tag{3.16}$$

$$\mathbf{y}^{k+1} = \mathbf{y}^k + \mu_k \mathbf{c}^{k+1} \tag{3.17}$$

CHAPTER 4

Experiments

The camera is first calibrated to obtain a homography mapping 3D world points to 2D pixel coordinates. Once the camera is calibrated, 30x30 pixel images are displayed on an LCD screen occluded from the camera's line of sight. The LCD screen is positioned so its normal vector is perpendicular to the wall (Figure 4.1). A laptop is used to control the LCD screen, and a DSLR camera with a rotatable polarization filter is offset from the screen and pointed towards the wall to obtain an image of the wall's irradiance distribution. Four images are recorded with the DSLR camera at four polarizing filter angles $(0°, 45°, 90°, 135°)$ and Equation 4.1 is used to calculate Stokes vectors for all camera pixels. With knowledge of scene geometry and intrinsic and extrinsic camera properties, the LTM is calculated via the modified Cook-Torrance shader. When combined with the DSLR polarization image, the inverse problem is solved for the monitor image. The diffuse surface used for tests was an office desk white laminate.

$$\mathbf{S} = \begin{pmatrix} \frac{1}{2}[I(0°) + I(45°) + I(90°) + I(135°)] \\ I(0°) - I(90°) \\ I(45°) - I(135°) \end{pmatrix} \tag{4.1}$$

4.0.1 Light Transport Matrix is Sparse in Polarization Domain

The two ground truth images in Figure 4.2 appear identical. However, they differ slightly. The top image's black pixels are assumed to have zero intensity which represent an ideal monitor with true black, while the bottom image's black pixels have intensities equal to 0.07 similar to real monitors. While this small change causes the polarization LTM to become

Figure 4.1: Experimental setup with monitor illuminating diffuse surface and DSLR camera with polarizing filter imaging illuminated region on wall
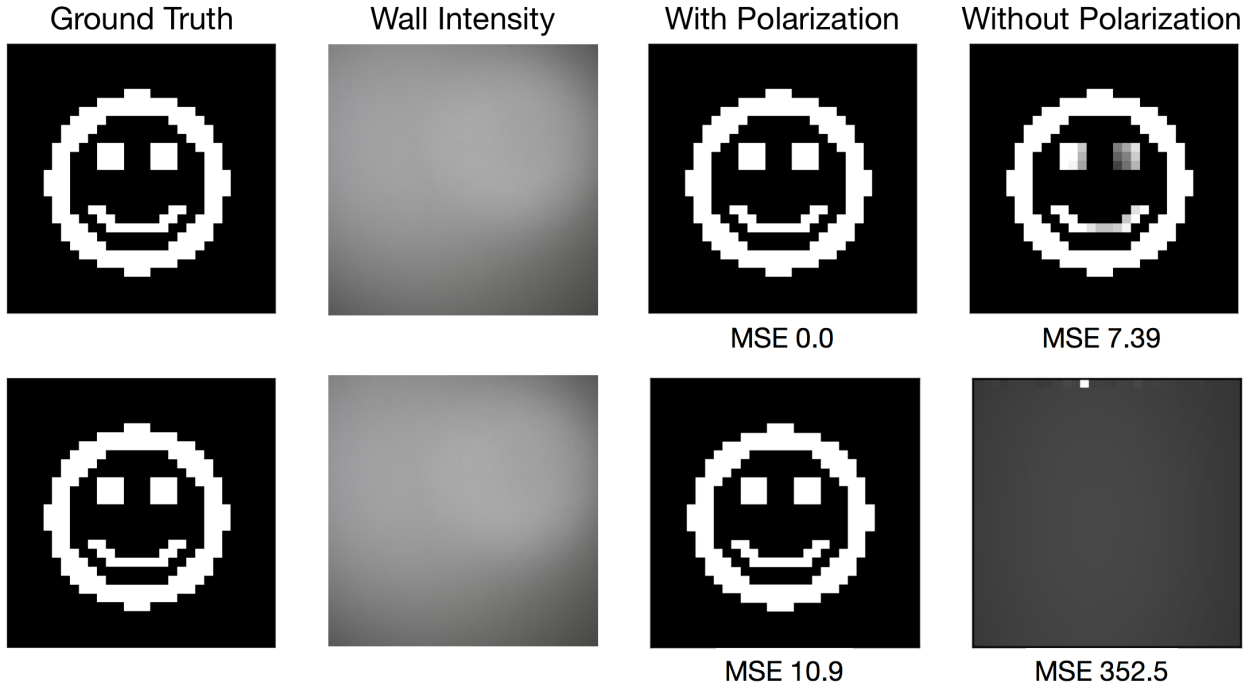
Figure 4.2: Two similar monitor images have largely different effects on NLOS imaging. The top image has black pixel intensities of 0 (sparse light transport) while the bottom has intensities of 0.07 (dense light transport). While intensity fails under these conditions, polarization NLOS method is robust.

more ill-conditioned than the intensity LTM, it maintains a 63% sparsity while the intensity LTM becomes 100% dense. This suggests that under certain conditions, NLOS imaging in the polarization domain can have beneficial properties that make solving the inverse problem easier.

4.0.2 Polarization-Based NLOS has Difficulty Matching Colors

Polarization-based NLOS imaging experiments was also conducted on colorful scenes to test its ability to discriminate between different hues. Figure 4.3 shows the 8-bit art used for these tests which include a coin, a wrapped piece of candy, and an angry pumpkin. The method proposed in this paper replicates the shape well and captures some shading detail distinguishing the center from the outer ring. However, it fails to apply a the gradient from top to bottom to resemble overhead lighting. Both the polarization and intensity approaches recovered the yellow region of the candy wrapper, but both failed to produce an image with features resembling the round center or twisted ends. The nature of this image is related to that of the modified smiley due to the two large regions of uniformly colored dark grey pixels. Both methods worked well in replicating the pumpkin's facial features. However, it appears as though they both have issues distinguishing between the pumpkin and the gradient background, and their solutions are to blend the regions even though they are clearly two different colors. However, the polarization-based image is noticeably flatter than the intensity-based image, which is true for all three color images.

4.0.3 Alternative Regularization Methods should be Explored

Tikhonov regularization was employed to encourage the selection of the smallest intensities that still satisfy the light transport. However, this regularly overpowered the least squares solution and produced pixel intensity estimates much lower than the ground truth as evident in Figure 4.4. When NLOS polarization results are compared to those of pure intensity, the Tikhonov-regularized polarization-based solutions are much brighter. This is due to the use of an uncommon Tikhonov matrix form that directly regularizes only the polarization s_0

Ground Truth	Wall Intensity	With Polarization	Without Polarization
		MSE 54.2	MSE 48.1
		MSE 202.4	MSE 129.5
		MSE 133.0	MSE 86.0

Figure 4.3: The intensity-based algorithm outperforms polarization-based methods at recovering color channels and tends to retain more shading information. Pumpkin by

| | Ground Truth | Wall Intensity | With Polarization | Without Polarization |

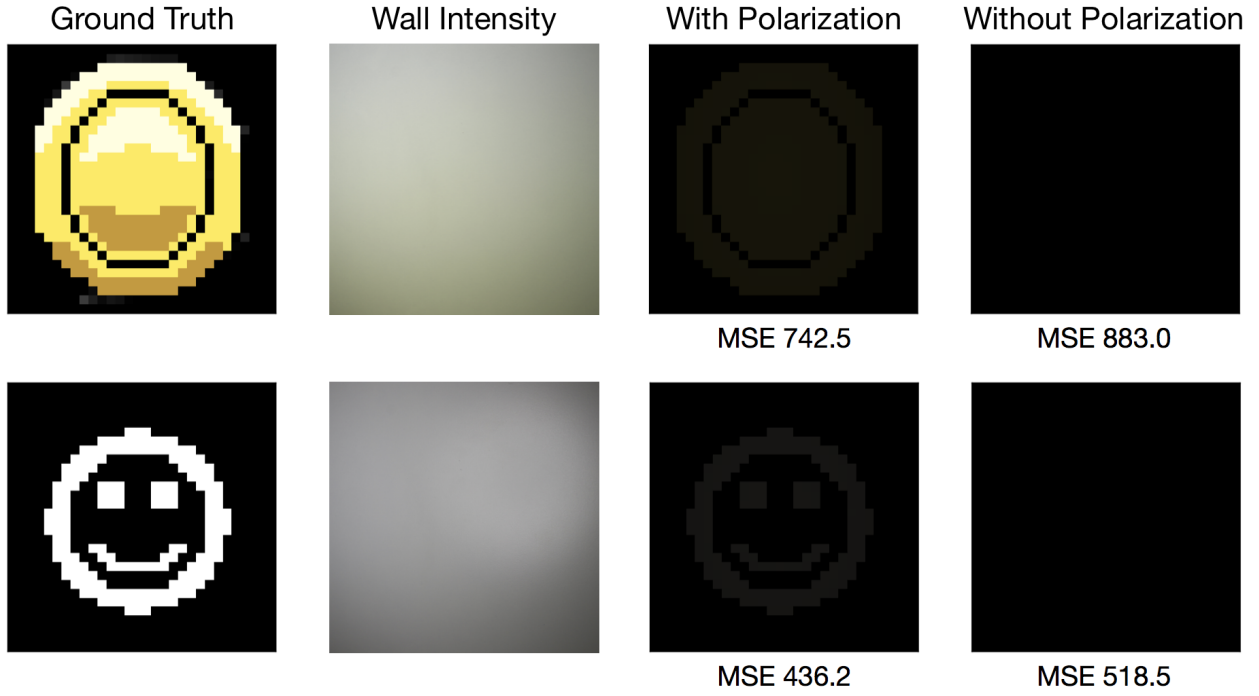MSE 742.5   MSE 883.0

MSE 436.2   MSE 518.5

Figure 4.4: NLOS monitor image estimation using Tikhonov regularization underestimates true monitor pixel values. Results using polarization are lightly visible while the intensity-based estimate is indistinguishable from the background

intensities, affecting s_1 and s_2 indirectly and loosely via relational constraints. This loose coupling of the Tikhonov matrix to the extra dimensionality of the polarization representation over scalar intensity enabled it to adjust and counteract the negative effects of the Tikhonov regularization.

CHAPTER 5

Conclusion

In this paper, the Cook-Torrance shader was leveraged to model diffuse polarized reflections from rough surfaces by replacing reflectances with Mueller matrices and intensities with Stokes vectors. That model was then used to calculate the light transport for NLOS imaging of an occluded monitor using a low-cost consumer-grade DSLR camera with a rotating polarizing filter. NLOS imaging with diffuse reflections naturally renders a dense light transport matrix that makes the inverse problem intractable.

Benefits Polarization-informed NLOS imaging has the benefit of extracting more information from the environment while also having a sparse transport matrix. This advantage was demonstrated in the case where the intensity-based NLOS failed to estimate the occluded monitor image while the polarization-based approach estimated it with little error.

Drawbacks Those benefits come at the cost of a longer data collection period requiring four photos for each single photo necessary for a pure intensity approach. Another drawback is the added complexity constraints and regularization introduce that are necessary to manage the realizability of the estimated Stokes vectors.

Future Work The combination of polarization with NLOS imaging has many applications. Rather than using polarization to aid in estimating intensities, the polarization information can be used directly to recover the polarization state of a hidden light source for classification purposes. These methods may also be able to determine whether an occluded light source is pointed directly at the wall or if the light is undergoing multiple reflections prior to observation. This could help in safety situations to make inferences about an unknown

environment. Finally, if shape from polarization can be carried out via NLOS, this would greatly improve the capability of passive NLOS imaging systems.

REFERENCES

[1] Smith, B. M., O'Toole, M., and Gupta, M., "Tracking Multiple Objects Outside the Line of Sight Using Speckle Imaging," *Proceedings of the IEEE Conference on Computer Vision and Pattern Recognition*, 2018, pp. 6258–6266.

[2] Katz, O., Heidmann, P., Fink, M., and Gigan, S., "Non-invasive single-shot imaging through scattering layers and around corners via speckle correlations," *Nature photonics*, Vol. 8, No. 10, 2014, pp. 784.

[3] Heide, F., OToole, M., Zang, K., Lindell, D. B., Diamond, S., and Wetzstein, G., "Non-line-of-sight Imaging with Partial Occluders and Surface Normals," *ACM Trans. Graph.*, 2019.

[4] Lindell, D. B., Wetzstein, G., and OToole, M., "Wave-based non-line-of-sight imaging using fast f-k migration," *ACM Trans. Graph. (SIGGRAPH)*, Vol. 38, No. 4, 2019, pp. 116.

[5] Saunders, C., Murray-Bruce, J., and Goyal, V. K., "Computational periscopy with an ordinary digital camera," *Nature*, Vol. 565, No. 7740, 2019, pp. 472.

[6] Bouman, K. L., Ye, V., Yedidia, A. B., Durand, F., Wornell, G. W., Torralba, A., and Freeman, W. T., "Turning corners into cameras: Principles and methods," *Proceedings of the IEEE International Conference on Computer Vision*, 2017, pp. 2270–2278.

[7] Tancik, M., Swedish, T., Satat, G., and Raskar, R., "Data-Driven Non-Line-of-Sight Imaging With A Traditional Camera," *Imaging Systems and Applications*, Optical Society of America, 2018, pp. IW2B–6.

[8] Treibitz, T. and Schechner, Y. Y., "Active polarization descattering," *IEEE transactions on pattern analysis and machine intelligence*, Vol. 31, No. 3, 2008, pp. 385–399.

[9] Kadambi, A., Taamazyan, V., Shi, B., and Raskar, R., "Polarized 3D: High-Quality Depth Sensing with Polarization Cues," *International Conference on Computer Vision (ICCV)*, 2015.

[10] Han, T., Yao, M., Han, G., Wang, T., Jiang, J., and Xu, K., "Study on the cross-polarization method for extracting internal information of objects," *Optik*, Vol. 180, 2019, pp. 433–441.

[11] Bruce, N., "Calculations of the Mueller matrix for scattering of light from two-dimensional surfaces," *Waves in random media*, Vol. 8, No. 1, 1998, pp. 15–28.

[12] Letnes, P. A., Maradudin, A. A., Nordam, T., and Simonsen, I., "Calculation of the Mueller matrix for scattering of light from two-dimensional rough surfaces," *Physical Review A*, Vol. 86, No. 3, 2012, pp. 031803.

[13] Thorsos, E. I., "The validity of the Kirchhoff approximation for rough surface scattering using a Gaussian roughness spectrum," *The Journal of the Acoustical Society of America*, Vol. 83, No. 1, 1988, pp. 78–92.

[14] Wang, X., Wang, L. V., Sun, C.-W., and Yang, C. C., "Polarized light propagation through scattering media: time-resolved Monte Carlo simulations and experiments," *Journal of biomedical optics*, Vol. 8, No. 4, 2003, pp. 608–618.

[15] Elfouhaily, T. M., Guérin, C.-A., et al., "A critical survey of approximate scattering wave theories from random rough surfaces," *Waves in Random Media*, Vol. 14, No. 4, 2004, pp. R1–R40.

[16] Blinn, J. F., "Models of light reflection for computer synthesized pictures," *ACM SIGGRAPH computer graphics*, Vol. 11, ACM, 1977, pp. 192–198.

[17] Phong, B. T., "Illumination for computer generated pictures," *Communications of the ACM*, Vol. 18, No. 6, 1975, pp. 311–317.

[18] Oren, M. and Nayar, S. K., "Generalization of Lambert's reflectance model," *Proceedings of the 21st annual conference on Computer graphics and interactive techniques*, ACM, 1994, pp. 239–246.

[19] Cook, R. L. and Torrance, K. E., "A reflectance model for computer graphics," *ACM Transactions on Graphics (TOG)*, Vol. 1, No. 1, 1982, pp. 7–24.

[20] Fang, E. X., He, B., Liu, H., and Yuan, X., "Generalized alternating direction method of multipliers: new theoretical insights and applications," *Mathematical programming computation*, Vol. 7, No. 2, 2015, pp. 149–187.